

The influence of frequency-dependent radiative transfer on the structures of radiative shocks

N. Vaytet^{1,*}, M. González², E. Audit^{3,4}, G. Chabrier^{1,5}

¹École Normale Supérieure de Lyon, CRAL, UMR CNRS 5574, Université de Lyon, 46 Allée d'Italie, 69364 Lyon Cedex 07, France

²Université Paris Diderot, Sorbonne Paris Cité, AIM, UMR 7158, CEA, CNRS, F-91191 Gif-sur-Yvette, France

³Maison de la Simulation, USR 3441, CEA - CNRS - INRIA - Université Paris-Sud - Université de Versailles, F-91191 Gif-sur-Yvette, France

⁴CEA/DSM/IRFU, Service d'Astrophysique, Laboratoire AIM, CNRS, Université Paris Diderot, F-91191 Gif-sur-Yvette, France

⁵School of Physics, University of Exeter, Exeter, EX4 4QL, UK

6 Mar 2013

arXiv:1303.1385v1 [astro-ph.HE]

ARTICLE INFO

Article history:

Received 7 November 2012

Accepted 6 March 2013

Available online 7 March 2013

Keywords:

Radiative transfer

Moment model

Multigroup

Laboratory astrophysics

Numerical methods

Shock waves

ABSTRACT

Radiative shocks are shocks in a gas where the radiative energy and flux coming from the very hot post-shock material are non-negligible in the shock's total energy budget, and are often large enough to heat the material ahead of the shock. Many simulations of radiative shocks, both in the contexts of astrophysics and laboratory experiments, use a grey treatment of radiative transfer coupled to the hydrodynamics. However, the opacities of the gas show large variations as a function of frequency and this needs to be taken into account if one wishes to reproduce the relevant physics. We have performed radiation hydrodynamics simulations of radiative shocks in Ar using multigroup (frequency dependent) radiative transfer with the HERACLES code. The opacities were taken from the ODALISC database. We show the influence of the number of frequency groups used on the dynamics and morphologies of subcritical and supercritical radiative shocks in Ar gas, and in particular on the extent of the radiative precursor. We find that simulations with even a low number of groups show significant differences compared to single-group (grey) simulations, and that in order to correctly model such shocks, a minimum number of groups is required. Results appear to eventually converge as the number of groups increases above 50. We were also able to resolve in our simulations of supercritical shocks the adaptation zones which connect the cooling layer to the final post-shock state and the precursor. Inside these adaptation zones, we find that the radiative flux just ahead of the shock in one or several high-opacity groups can heat the gas to a temperature higher than the post-shock temperature. Through the use of Hugoniot curves, we have checked the consistency of our radiation hydrodynamics scheme by showing that conservation of mass, momentum and energy (including radiative flux) holds throughout the computational domain for all our simulations. We conclude that a minimum number of frequency groups are required to correctly simulate radiating flows in gases whose opacities present large variations as a function of frequency.

1 Introduction

Radiative shocks are shocks in a gas where the radiative energy and flux coming from the very hot post-shock material are non-negligible in the shock's total energy budget (Zel'dovich & Raizer 1967; Mihalas & Mihalas 1984). A radiative precursor is formed ahead of the shock when the forward flux of ionizing photons exceeds the flux of atoms approach-

ing the shock front. These conditions are met when the shock velocity exceeds the threshold required to produce the necessary photon flux (Keiter et al. 2002). Two regimes of radiative shocks are often described in the literature. The first is called the subcritical regime, where the shock has only a transmissive precursor and the temperature just ahead of the discontinuity is not equal to the final downstream state temperature. The second is known as the supercritical

*Corresponding author. E-mail address: neil.vaytet@ens-lyon.fr

regime which arises as the strength of the shock increases; a diffusive region in the precursor appears and the pre-shock temperature reaches the final state temperature (see Drake 2006, for more details).

The classical structure of a subcritical radiative shock is depicted in Fig. 1a. The preshock gas is heated by the radiative precursor to a temperature T_- and the shock compression heats it further to a temperature T_+ which is higher than the final post-shock equilibrium state T_1 . The gas then cools down inside the cooling layer to reach the equilibrium state T_1 by radiating the excess energy away. The radiation is decoupled from the gas inside the cooling layer and the transmissive precursor. The pressure gradient in the precursor, through the conservation of mass and momentum, causes the velocity to decrease and the density to increase to a value ρ_- ahead of the discontinuity. The sharp density jump of the shock from ρ_- to ρ_+ then takes place on the gas viscous scale. The density increases further from ρ_+ to ρ_1 inside the cooling layer as the gas contracts (see also Zel'dovich & Raizer 1967; Drake 2006).

In the case of an optically thick supercritical radiative shock (shown in Fig. 1b), we have $T_- \approx T_1$. The radiative temperature is equal to the gas temperature for the most part, except that it remains constant across the cooling layer and is higher than the gas temperature inside the transmissive precursor (Mihalas & Mihalas 1984). As stated above, the pressure gradient at the head of the precursor causes the density to increase. Since the gas temperature is close to being constant in the diffusive part of the precursor, there is no more pressure gradient and the density reaches a plateau value ρ_- ahead of the discontinuity.

The study of radiative shocks begun in the late 1940s with theoretical studies on the Rankine-Hugoniot jump conditions including a non-negligible radiation pressure for very energetic shocks (see Blinnikov & Tolstov 2011, for a short review). The studies were very rapidly pursued and extended in the field of astrophysics since no processes on Earth could achieve high enough energies to produce such shocks. Radiative shocks are indeed found in novae (Vaytet et al. 2007; Orlando et al. 2009; Bode & Evans 2008), supernovae (Draine & McKee 1993; Ghavamian et al. 2000; Nymark et al. 2006), stellar atmospheres (Faddeyev & Gillet 2000; Gillet 2006), accretion processes in star formation (Stahler et al. 1980; Commerçon et al. 2011), symbiotic stars (Falize et al. 2009; Imamura 1985) and jets (Raga et al. 1999; Reipurth & Raga 1999). This omnipresence makes them a key physical process at the heart of high energy astrophysics, and it is thus essential to fully understand the details of such a mechanism.

In recent years, with the modern advances in technology, radiative shocks have been produced in a number of laboratory laser facilities (see Bosier et al. 1986; Edwards et al. 2001; Fleury et al. 2002; Reighard et al. 2006; Busquet et al. 2007; Michaut et al. 2009, for example), where very high-energy lasers are used to drive radiative shocks inside gas chambers. This allows new diagnostics of the properties of radiative shocks with a much more detailed view than

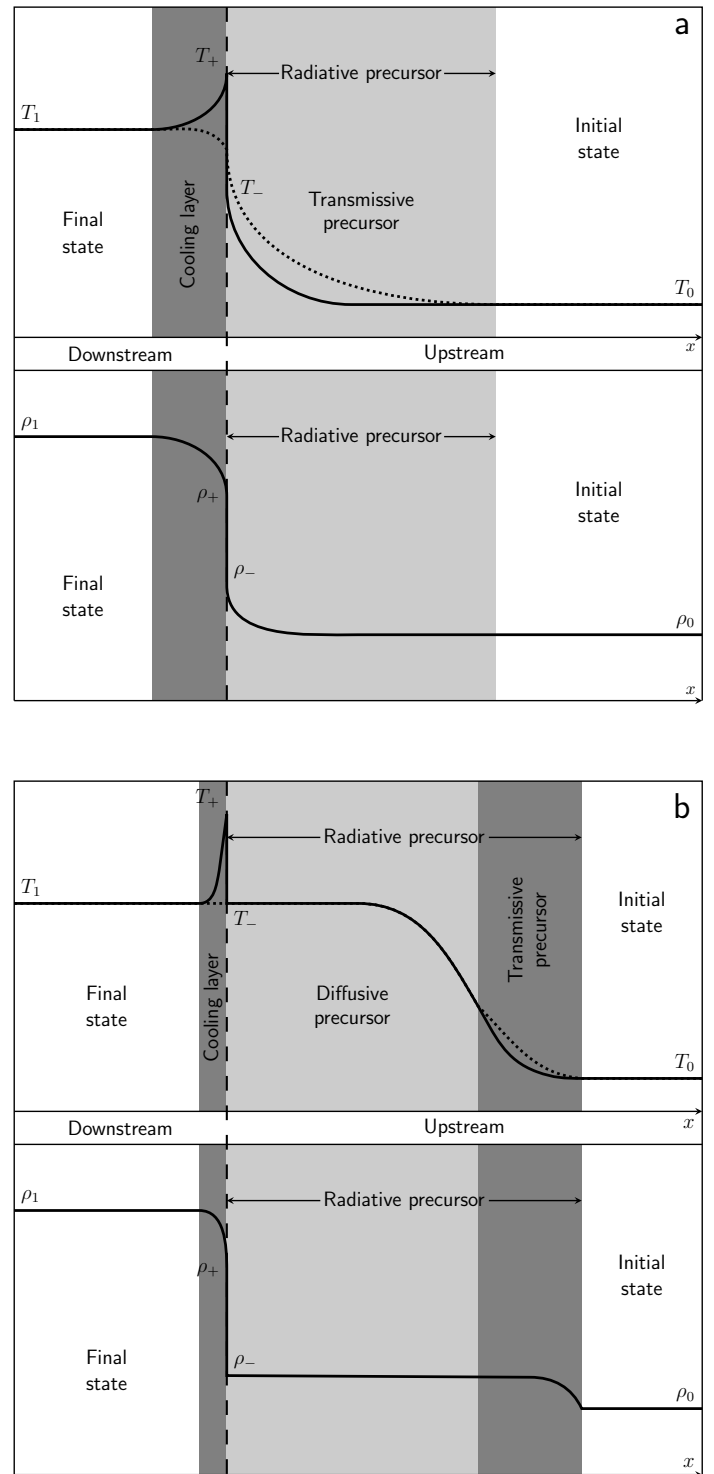


Figure 1: Classical structure of a subcritical (a) and supercritical (b) radiative shock. The direction of the gas flow is from right to left in the frame where the shock is at rest. The panels show the gas (solid) and radiative (dotted) temperature (top) and the gas density (bottom) as a function of distance in each case. The position of the temperature and density jumps is marked by the vertical dashed line. The relative sizes of the layers are for illustration purposes only.

would ever be possible in astrophysics. Radiative shock experiments allow for the validation of numerical simulations

which are overwhelmingly used in high-energy physics and astrophysics to make predictions on high-energy flows.

Semi-analytic studies of the structure of radiative shocks have been carried out by [Lowrie & Rauenzahn \(2007\)](#); [Lowrie & Edwards \(2008\)](#), and several comparisons between experiments and simulations have also been undertaken by [Bouquet et al. \(2004\)](#); [Leibrandt et al. \(2005\)](#); [Reighard et al. \(2007\)](#); [González et al. \(2009\)](#), for example. One key piece of data that is required by the numerical simulations in order to accurately model the flow is the opacities of the gas in which the shock is launched. Gas opacities show large variations as a function of temperature and density as well as frequency, and including detailed opacities in simulations have crucial effects on the structures of radiative shocks. [Vaytet et al. \(2011\)](#) performed simulations of a radiative shock in Xe using a realistic opacity set and showed the importance of taking into account the frequency dependence of the opacities, rather than simply integrating over all frequencies, as is commonly done in simulations of radiative shocks

This paper aims to build on the idea that a frequency dependent treatment of radiative transfer is crucial in simulations of radiative shocks. In particular, we experiment further with the multigroup method of [Vaytet et al. \(2011\)](#) by studying the effect of the number of frequency groups on the structures of the radiative shocks (mainly the variations in size of the precursor). We performed simulations of stationary radiative shocks (both sub- and supercritical) using 1 to 100 frequency groups, and the differences between the results are discussed. The opacities are a crucial part of the radiative transfer model; they govern the amount of energy that will be absorbed and emitted by the gas and can hence determine the structure of the flow. Laboratory experiments use high atomic number gases to launch radiative shocks to take advantage of the strong gas heating due to the lower heat capacity. Common choices are argon (Ar) and xenon inert gases, and in this work we have chosen to use Ar (see section 2.5 for more details).

2 The multigroup RHD simulations of radiative shocks

2.1 Radiative transfer

We use the M_1 moment model ([Levermore 1984](#); [Dubroca & Feugeas 1999](#)) to approximate the equation of radiative transfer. The M_1 method uses the first two moment equations governing the evolution of the radiative energy and flux

$$\begin{aligned} \partial_t E + \nabla \cdot \mathbf{F} &= \sigma(4\pi B - cE) \\ \partial_t \mathbf{F} + c^2 \nabla \cdot \mathbb{P} &= -\sigma c \mathbf{F} \end{aligned} \quad (1)$$

where c is the speed of light, σ the absorption/emission coefficient and B the black body specific intensity. E , \mathbf{F} , and \mathbb{P} are the zeroth, first and second moments of the radiation specific intensity, namely the radiative energy density, the radiative energy flux, and the radiative pressure, respectively. In order to close system (1), the radiative pressure is expressed as a function of the radiative energy and flux following $\mathbb{P} = \mathbb{D}E$ where \mathbb{D} is known as the Eddington tensor. The expression

for \mathbb{D} is obtained by minimizing the radiative entropy which yields

$$\mathbb{D} = \frac{1 - \chi}{2} \mathbb{I} + \frac{3\chi - 1}{2} \frac{\mathbf{F} \otimes \mathbf{F}}{\|\mathbf{F}\|^2} \quad (2)$$

where

$$\chi = \frac{3 + 4f^2}{5 + 2\sqrt{4 - 3f^2}} \quad (3)$$

and $f = \|\mathbf{F}\|/cE$ is known as the reduced flux. Note that by definition of E and \mathbf{F} , we have $f \leq 1$, which implies that the radiative energy is transported at most at the speed of light. In one dimension we simply have $P = \chi E$. This closure relation recovers the two asymptotic regimes of radiative transfer. In the free-streaming limit (i.e. transparent media), we have $f = 1$ and $\chi = 1$. On the other hand, in the diffusion limit, $f = 0$ and $\chi = 1/3$, which corresponds to an isotropic radiation pressure.

2.2 The equations of multigroup radiation hydrodynamics

We use the multigroup version of the M_1 model coupled to the gas hydrodynamics described in [Vaytet et al. \(2011\)](#) to account for frequency dependence of the absorption and emission coefficients (see [Shestakov & Offner 2008](#); [van der Holst et al. 2011](#); [Zhang et al. 2013](#), for other examples of Godunov multigroup methods). In the multigroup model, the equations of radiative transfer are integrated into a finite number of frequency bins (or groups) and the opacities are averaged over the same frequency ranges. The closure relation 3 is applied within each frequency group. The more the frequency groups, the more accurate the methods becomes, but the higher the computational cost. The system of multigroup RHD equations in the comoving frame is

$$\partial_t \rho + \nabla \cdot (\rho \mathbf{u}) = 0 \quad (4)$$

$$\partial_t (\rho \mathbf{u}) + \nabla \cdot (\rho \mathbf{u} \otimes \mathbf{u} + p \mathbb{I}) = \sum_{g=1}^{Ng} (\sigma_{Fg}/c) \mathbf{F}_g \quad (5)$$

$$\begin{aligned} \partial_t e + \nabla \cdot (\mathbf{u}(e + p)) &= \sum_{g=1}^{Ng} \left[c(\sigma_{Eg} E_g - \sigma_{Pg} \Theta_g(T)) \right. \\ &\quad \left. + (\sigma_{Fg}/c) \mathbf{u} \cdot \mathbf{F}_g \right] \end{aligned} \quad (6)$$

$$\begin{aligned} \partial_t E_g + \nabla \cdot \mathbf{F}_g + \nabla \cdot (\mathbf{u} E_g) + \mathbb{P}_g : \nabla \mathbf{u} \\ - \nabla \mathbf{u} : \int_{\nu_{g-1/2}}^{\nu_{g+1/2}} \partial_\nu (\nu \mathbb{P}_\nu) d\nu &= c(\sigma_{Pg} \Theta_g(T) - \sigma_{Eg} E_g) \end{aligned} \quad (7)$$

$$\begin{aligned} \partial_t \mathbf{F}_g + c^2 \nabla \cdot \mathbb{P}_g + \nabla \cdot (\mathbf{u} \otimes \mathbf{F}_g) + \mathbf{F}_g \cdot \nabla \mathbf{u} \\ - \nabla \mathbf{u} : \int_{\nu_{g-1/2}}^{\nu_{g+1/2}} \partial_\nu (\nu \mathbb{Q}_\nu) d\nu &= -\sigma_{Fg} c \mathbf{F}_g \end{aligned} \quad (8)$$

where c is the speed of light, and ρ , \mathbf{u} , p and e are the gas density, velocity, pressure and total energy, respectively. \mathbb{Q}_ν is the third moment of the radiation specific intensity; the radiative heat flux. Subscripts ν denote monochromatic quantities, and we also define

$$X_g = \int_{\nu_{g-1/2}}^{\nu_{g+1/2}} X_\nu d\nu \quad (9)$$

which represents for $X = E$, \mathbf{F} , \mathbb{P} the radiative energy, flux and pressure inside each group g which holds frequencies

between $v_{g-1/2}$ and $v_{g+1/2}$. N_g is the total number of groups and $\Theta_g(T)$ is the energy of the photons having a Planck distribution at temperature T inside a given group. The quantities σ_{Pg} , σ_{Eg} and σ_{Fg} are the means of the absorption/emission coefficient σ_ν inside a given group weighted by the Planck function, the radiative energy and the radiative flux, respectively. The radiative quantities are expressed in the frame comoving with the fluid, which allows simple expressions to be used for the source terms on the right hand side of equations (5)–(8). The terms involving the frequency derivatives of the radiative pressure and heat flux $\partial_\nu(\nu P_\nu)$ and $\partial_\nu(\nu Q_\nu)$ are solved using a finite volume method in the frequency dimension (see Vaytet et al. 2011, for details).

2.3 Numerical method

We have implemented the multigroup radiative transfer module of Vaytet et al. (2011) in the 3D radiation hydrodynamics second order Godunov code HERACLES[†] (González et al. 2007). It uses an explicit solver for the hydrodynamics and an implicit solver for the radiative transfer. The Ar gas equation of state is a simple modified ideal gas equation of state; the ionization energy is neglected but the ionization state is used to compute the mean molecular weight which in turn affects the gas temperature. The disregard of the ionization energy may greatly over-estimate the temperature (ionization can represent half of the internal energy for mid- to highly ionized flows; Drake 2006), but since we focus solely on the differences between mono- and multi-frequency radiative transfer methods and no comparison between simulations and experiments is made throughout, this oversight does not matter for the purposes of the present paper.

In the RHD equations, it is not trivial to compute the radiative energy and flux-weighted mean opacities σ_{Eg} and σ_{Fg} . Common practise is to set $\sigma_{Eg} = \sigma_{Pg}$ and $\sigma_{Fg} = \sigma_{Rg}$ where σ_R is the Rosseland mean opacity. In this work, we have used an average opacity $\sigma_{Eg} = \sigma_{Fg} = \sigma_{Ag}$ which varies between the values of σ_{Pg} and σ_{Rg} depending on the reduced flux f (see Appendix A for more details). However, we wish to point out that the inaccuracies which arise from these different approximations are reduced as the number of frequency groups used increases, since in the limit of infinite frequency resolution, all of these quantities simply reduce to σ_ν . Any approximation is thus less crude in a multigroup model than in a grey model. The simulations were run on a varying number of CPUs ranging from 12 for the low numbers of frequency groups to 200 for the heavier calculations.

2.4 Initial and boundary conditions

The simulations of stationary radiative shocks were performed in a one-dimensional regular cartesian grid comprising 1000 cells (see Appendix B for a discussion on resolution). The grid sizes were $L = 1$ cm and $L = 6$ cm for the simulations of subcritical and supercritical radiative shocks, respectively. The discontinuity was initially located at $x_s = L/4$

Table 1: Simulation results

Run name	Number of groups	Shock velocity (km s ⁻¹)	Mach number	Shock position (cm)	Precursor size (cm)
SUB001	1			0.250	0.016
SUB005	5			0.250	0.025
SUB010	10	30	5.62	0.250	0.024
SUB020	20			0.250	0.052
SUB050	50			0.250	0.070
SUB100	100			0.250	0.073
SUP001	1			1.269	2.277
SUP005	5			1.245	2.475
SUP010	10	100	18.75	1.239	2.582
SUP020	20			1.233	2.650
SUP050	50			1.227	2.790
SUP100	100			1.227	2.811

Note: The position of the shock is defined as the position where the derivative of the velocity is the maximum. The size of the precursor is measured between the shock position and the first point (from the right hand side) where the gas temperature exceeds 1.1 eV.

and the gas to the right of the discontinuity was given a density of $\rho_0 = 10^{-3}$ g cm⁻³ and a temperature of $k_B T = 1$ eV. The radiative temperature was in equilibrium with the gas and the radiative flux was zero. The upstream velocity was set to $u_0 = -30$ km s⁻¹ in the subcritical case and $u_0 = -100$ km s⁻¹ for the supercritical shock. Once the upstream state was chosen, the downstream state was calculated using the Rankine-Hugoniot jump conditions for a radiating fluid (Mihalas & Mihalas 1984), which describe the conservation of mass, momentum and energy across the discontinuity. We find (using the appropriate states of ionisation) the downstream quantities for the subcritical shock to be $\rho_1 = 3.65 \times 10^{-3}$ g cm⁻³, $u_1 = -8.21$ km s⁻¹ and $k_B T_1 = 6.92$ eV. In the case of the supercritical shock, we obtain $\rho_1 = 3.97 \times 10^{-3}$ g cm⁻³, $u_1 = -25.18$ km s⁻¹ and $k_B T_1 = 32.85$ eV. The upstream and downstream values are also imposed inside ghost cells at the right and left boundaries of the computational domain, respectively. In computing the upstream and downstream states, we have assumed that we are sufficiently far from the shock so that the radiative temperature is in equilibrium with the gas temperature and that the radiative flux is zero, which is the case in our simulations.

2.5 The Argon opacities and the decomposition of the frequency domain

The opacities for the Ar gas were taken from the ODALISC[‡] database, which provides spectral opacities as well as mean opacities (Rosseland and Planck) of many elements for a wide range of physical conditions. We used the Ar opacities in the frequency range $h\nu = 1 - 16,000$ eV, computed with the POTREC code (Mirone et al. 1997) which is based on the

[†]http://irfu.cea.fr/Projets/Site_heracles/

[‡]<http://irfu.cea.fr/Projets/Odalisc/>

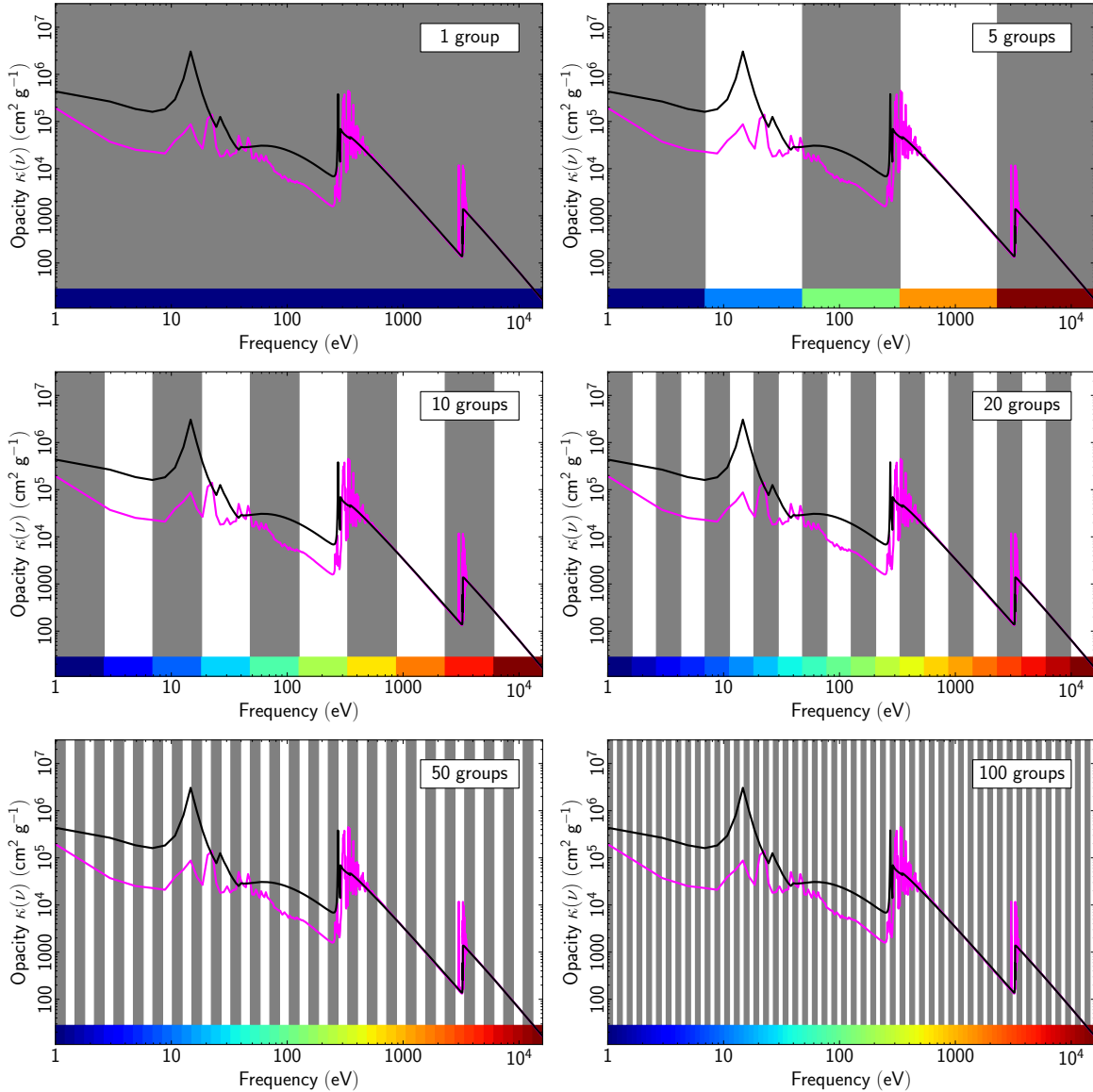


Figure 2: The Ar opacities with the decomposition of the frequency domain for 1 to 100 groups. The black line represents the opacities of the gas in the pre-shock (ρ, T) state while the magenta line is for the post-shock state of the supercritical case. The colour-bar at the bottom of each frame codes for the group number; this is used in Figs 3, 5 and 7.

average atom model, including l -splitting and $\Delta n = 0$ transitions. The spectral opacities for two different densities and temperature are shown in Fig. 2; the pre-shock state is represented by the black line ($\rho_0 = 10^{-3} \text{ g cm}^{-3}$; $k_B T_0 = 1 \text{ eV}$) while the magenta line is for the supercritical post-shock state ($\rho_1 \sim 4 \times 10^{-3} \text{ g cm}^{-3}$; $k_B T_1 \sim 33 \text{ eV}$). One can see that the opacities show important orders-of-magnitude variations as a function of frequency as well as gas density and temperature, and this can have a large impact on the results. A frequency-averaged model is in this case not an accurate approximation since it cannot model situations where a gas would be optically thick in one part of the spectrum and optically thin in another.

In this work, we performed simulations with 1, 5, 10, 20, 50 and 100 frequency groups. Choosing the appropriate decomposition of the frequency domain among the groups is

not very straightforward. Ideally, as soon as a large variation in κ_ν as a function of frequency is present, one would require a new frequency group. When only a small number of groups is used, different boundary choices can have different impacts on the simulation results. Group boundary placing naturally becomes less and less important as the number of frequency groups increases. For the benefit of a fair comparison between simulation results, the decomposition of the frequency domain among the groups was simply done logarithmically, as shown in Fig. 2.

3 Results

We performed simulations of subcritical and supercritical radiative shocks, using 1 – 100 frequency groups in both cases. The properties of the different runs are listed in Table 1.

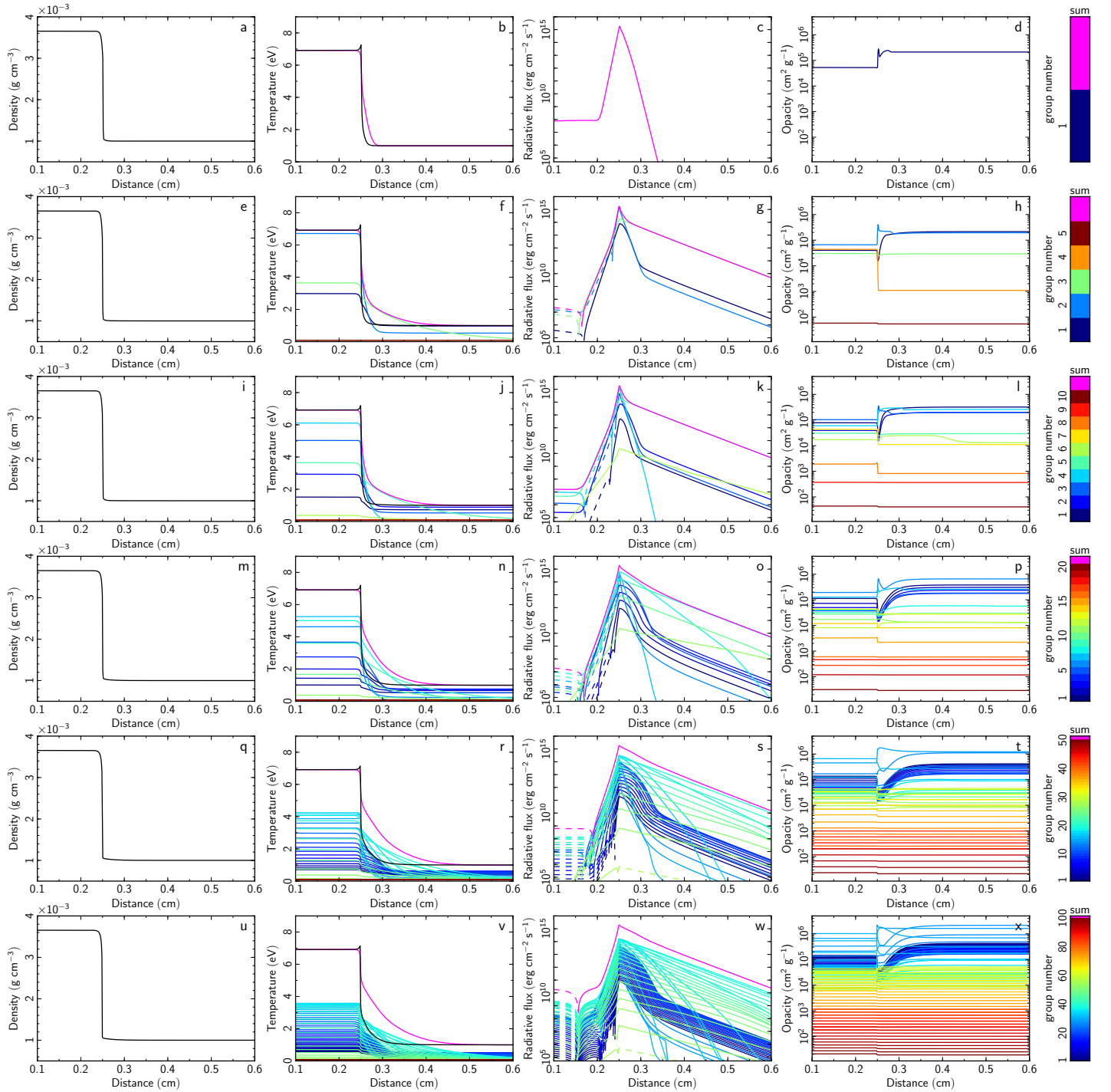


Figure 3: Stationary subcritical radiative shocks using (from top to bottom) 1 to 100 frequency groups. From left to right: gas density, gas (black) and radiative (colours) temperatures, radiative flux and gas opacity. At the end of each row is a colour bar coding for the different frequency groups. In the two central columns, the magenta curves represent the sum over all groups for the radiative temperature and flux. Dashed lines represent negative values of the radiative flux (i.e. flowing from right to left).

The initial discontinuity, set up with the Rankine-Hugoniot conditions described in 2.4, was left to evolve until all the structure in the radiative shock was fully developed and the stationary regime was reached. All the results shown below (apart from figures showing a time evolution) are in the

stationary regime.

3.1 The subcritical case

The results for the simulations of a subcritical radiative shock using 1 – 100 frequency groups are shown in Fig. 3.

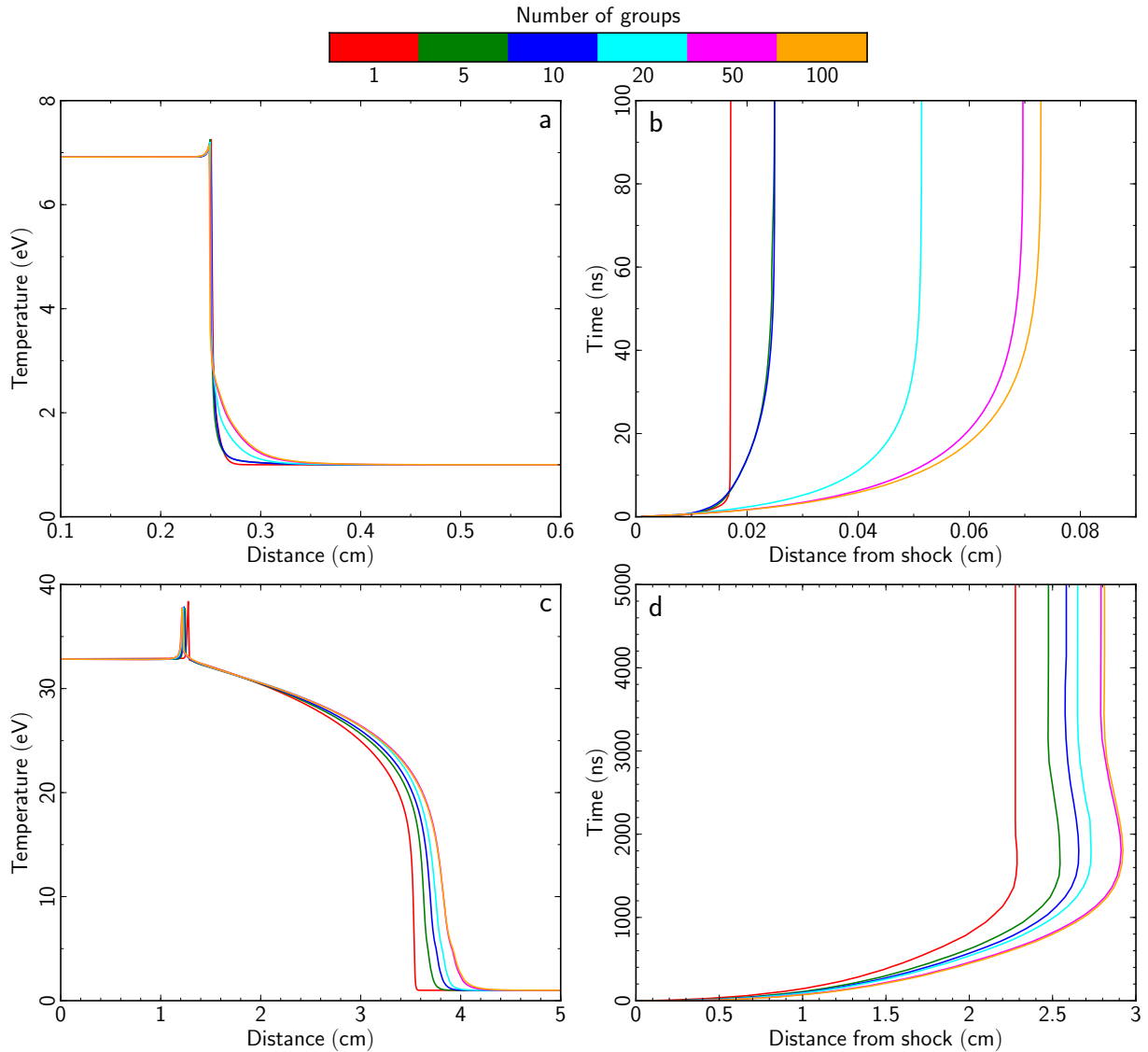


Figure 4: Left column: gas temperature as a function of distance using 1 – 100 frequency groups (see color legend at the top) in the case of subcritical (b) and supercritical (d) radiative shocks. Right column: distance between the head of the radiative precursor and the shock density jump in the case of subcritical (a) and supercritical (c) radiative shocks.

Each row is for a different number of groups. The columns from left to right display (as a function of distance) the gas density, the gas (black) and radiative (colours) temperatures, the radiative flux and the gas opacity. In the two middle columns, the magenta curves represent the sums over all groups.

We first take a look at the mono-group simulation; run SUB001 (top row). The profiles exhibit the classic structure of a subcritical radiative shock; a transmissive radiative precursor extends ahead of the shock heating the upstream gas and altering its density and velocity (not shown), the radiative flux (c) is maximum at the density jump (position of the hydrodynamic discontinuity) and we also note the presence of a cooling region (or Zel’dovich spike) in the temperature plot (b) at the position of the density jump, where the gas temperature exceeds the post-shock temperature. The precursor measures approximately 0.02 cm and the gas opacity

(which is averaged over the entire frequency range) lies between 5×10^4 and $3 \times 10^5 \text{ cm}^2 \text{ g}^{-1}$ throughout (note that the size of the precursor is measured between the shock position and the first point from the right hand side where the gas temperature exceeds 1.1 eV).

The first multigroup simulation was performed using 5 frequency groups (SUB005), the results of which are shown in the second row. The first major difference that emerges when compared to the grey simulation is that the extent of the radiative precursor has increased; even though the gas temperature profile has not changed significantly, the radiative temperature curve extends much further ahead of the discontinuity. This can be explained by the range of opacities observed in the different groups (see Fig. 3h), and in particular the opacity of group 3 (light green), whose radiative energy dominates inside the precursor, which is almost an order of magnitude lower than the grey average. The grey

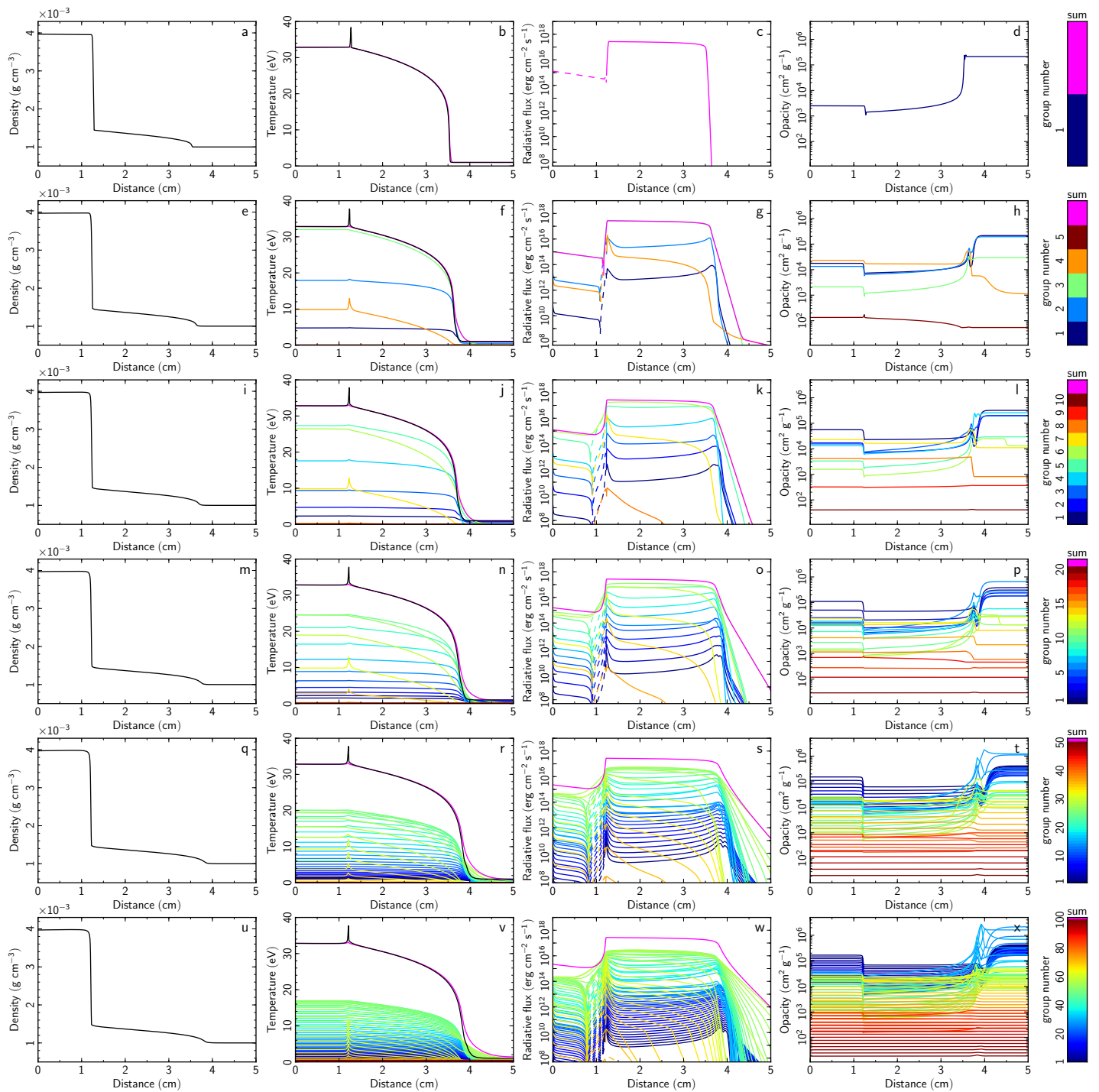


Figure 5: Same as Fig. 3 for the supercritical shock case.

opacity is biased towards a higher value which greatly affects the results, especially the radiative flux which now shows a long tail extending towards the right end of the simulation box.

The results of the subsequent runs, using 10, 20, 50 and 100 groups, are shown in the lower rows. While runs SUB005 and SUB010 are very similar to each other, the gas temperature profile has noticeably changed further in runs SUB020 to SUB100, this being most visible between 0.25

and 0.3 cm where the gas temperature is significantly altered by the radiation. The gas temperatures are overlaid inside the same window in Fig. 4a for a clearer view. The position of the density jump (or hydrodynamic shock) and the size of the precursor for all the simulations are listed in Table 1. The precursor sizes keep increasing with the number of frequency groups used. A greater resolution in the frequency domain allows an accurate treatment of the sharp slopes in the opacity curve (cf. Fig. 2), which affects

the amount of absorption ahead of the shock and defines the extent of the precursor. The extent of the precursor is plotted as a function of time in Fig 4b. The influence of the number of groups described above is very clear on this plot.

3.2 The supercritical case

The results for the simulations of a supercritical radiative shock using 1 – 100 frequency groups are shown in Fig. 5. The different rows and columns are identical to Fig. 3. The profiles are this time characteristic of a supercritical radiative shock; a diffusive radiative precursor strongly heats the gas ahead of the shock, notably altering the gas density, the post-shock gas and radiative temperatures are identical to the pre-shock ones and the Zel’dovich spike is clearly visible. As in the subcritical case, the size of the precursor increases with the number of frequency groups, growing by more than 20% between 1 and 100 groups, as explicated in Table 1 and illustrated in Figs 4c and 4d. The fact that there is very little difference between the 50 and 100-group simulations indicate that we have almost reached convergence of our results. The number of frequency groups used impacts the results less than in the subcritical case, since most of the radiative precursor is in the diffusive regime where the grey approximation is deemed to be accurate.

These findings have important consequences on predictions made by numerical simulations on the structure of radiative shocks. Indeed, due to the very different precursor sizes, studies of radiative shocks which make use of comparisons between observations and numerical calculations will most probably be inaccurate if a grey radiative transfer model is used. One can compare the right column of Fig. 4 to the shock-precursor position diagrams found in the literature (see Fig. 3 in Michaut et al. 2009 and Figs. 6 and 7 in González et al. 2006 for example).

3.3 Electron densities

In order to illustrate the differences between the grey and multigroup simulations further, we now consider the effects of our results on the observables commonly obtained in radiative shock experiments. We compare in Fig. 6 the evolution of the electron density N_e as a function of time and distance in the grey and the 100-group simulations for the subcritical (left column) and the supercritical shocks (right column). The middle panels (b), (c), (g) and (h) show the N_e distribution in the simulation frame. The dark red region is the post-shock final state with a dense and highly ionised medium, while the dark blue region is the pre-shock initial state. Between the two, the shock precursor is clearly visible in yellow. The sharp transition between the precursor (yellow) and the post-shock state (red) represents the position of the density jump as a function of time. The simulation frame panels are very useful in highlighting the differences between the grey and multigroup simulations; the radiative precursor is unmistakably larger in the multigroup case. The top panels (a) and (f) show a slice extracted from the simulation frame data, for an alternative view. We note that for the supercritical shock, the rightmost tip of the precursor is

much sharper in the grey than in the multigroup case. The supercritical simulation frame figures also reveal the slight displacement of the density jump towards the left, as the whole structure of the radiative shock develops over time.

The bottom panels (d), (e), (i) and (j) show the N_e distribution in the laboratory frame, and are reminiscent of Fig. 3 in Michaut et al. (2009). These simulated laboratory-frame diagnostics show that the differences between the grey and multigroup simulations would be large enough to be detected in experimental observations.

3.4 Detection of adaptation zones around the Zel’dovich temperature spike

We now turn to describe what is happening in the vicinity of the hydrodynamic discontinuity. Figure 7 shows a close-up around the Zel’dovich spike for runs (from left to right) SUP001, SUP005 and SUP100. The temperature profile of run SUP001 shows that the classic cooling layer structure, with a sharp edge on the right and a smooth cooling (or relaxation) region on the left (as depicted in Fig. ??), is almost resolved (see Appendix B for a discussion on resolution).

However, the temperature profile of run SUP005 shows a rather different structure, especially on the right hand side. There is a smooth region of ‘over-temperature’ to the right of the spike, spanning from $x = 1.26$ to 1.34 cm (indicated by arrow A1), where the gas temperature T_g is above the radiation temperature and higher than the final equilibrium temperature T_1 . It progressively returns to the same value as the radiation temperature as we move away from the spike towards the right. In a supercritical radiative shock, the pre-shock gas temperature cannot in principle exceed the post-shock temperature (Zel’dovich & Raizer 1967). The solutions are converged in both cases and the radiative precursors do not extend out to the right edge of the box. This effect must have another origin.

Looking at the radiative fluxes (panels g and h), we can see that in run SUP001, the flux shows a plateau right after the discontinuity. In SUP005, the same is observed for the dominant group 3 (light green) but group 4 (orange) does not show a plateau to the right of the shock, instead it decreases smoothly as we move away from the shock (see arrow A2). This indicates that the radiation in group 4 is being absorbed by the material to the right of the shock. Indeed, the group 4 opacity of the pre-shock material (panel n) is about an order of magnitude higher than the grey average in SUP001 (panel m) where the radiation can escape ‘freely’.

It appears that the high opacity in group 4 causes the pre-shock material to absorb the radiation in that group only, and this consequently heats up the gas a little more. It is like having a small precursor inside a precursor. This can be understood in terms of the following. A small amount of incident radiation energy absorbed by gas per unit angle, time, area and frequency is equal to the specific intensity loss, i.e.

$$dE_\nu^{\text{abs}} = -dI_\nu \cos \vartheta dA d\omega dt dv \quad (10)$$

which for a constant opacity along direction s becomes

$$dE_\nu^{\text{abs}} = \kappa_\nu I_\nu \cos \vartheta dA d\omega dt dv ds \quad (11)$$

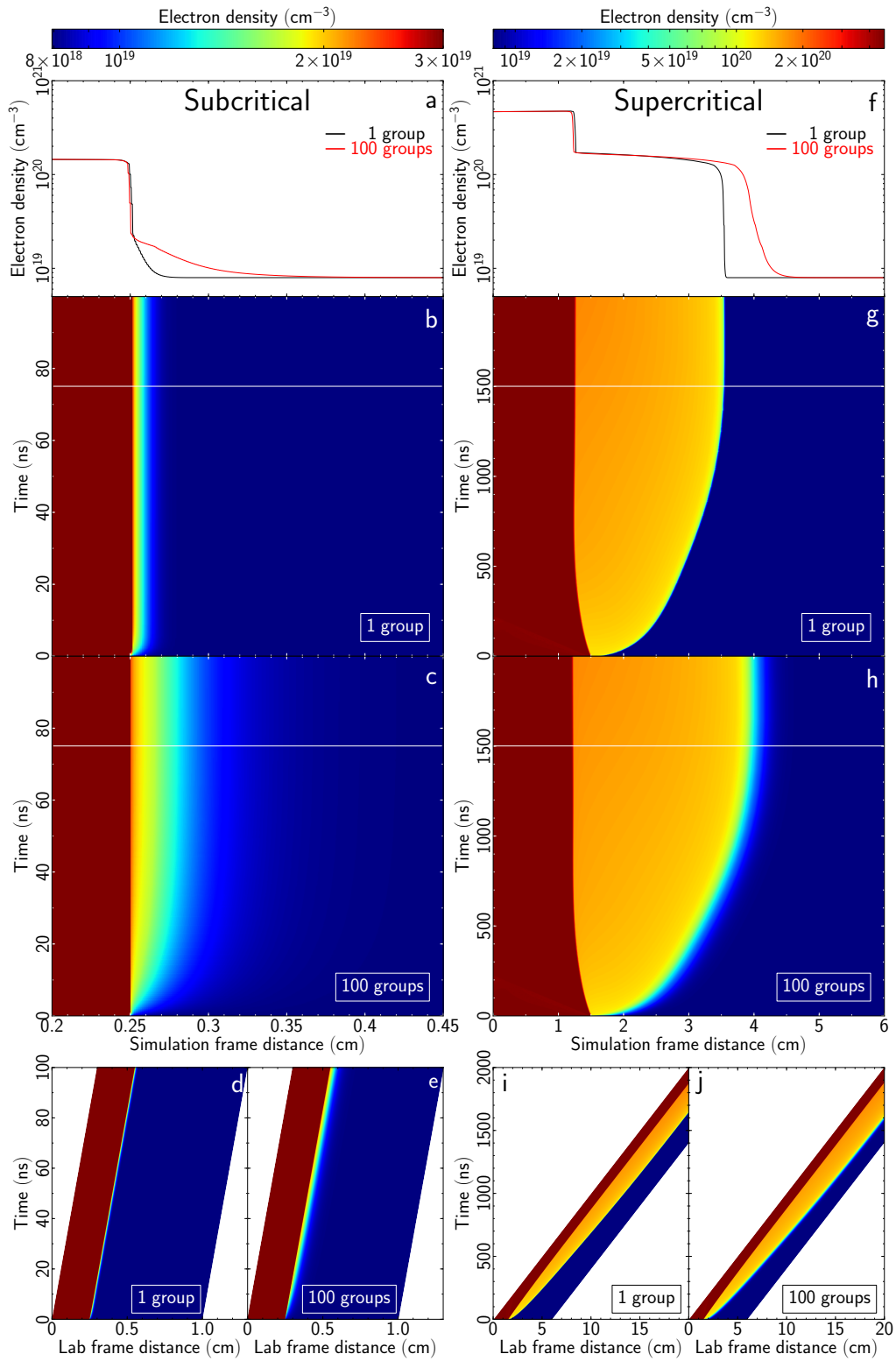


Figure 6: Time evolution of the electron density (N_e) as a function of distance for the subcritical case (left column) and the supercritical case (right column) using 1 and 100 frequency groups. Panels (a) and (f) show a slice through the 1 (black) and 100 (red) groups simulation rest frame data. Panels (b) and (g) show the distribution of N_e in the simulation frame for 1 group while panels (c) and (h) are for the 100-group case. The bottom row displays the N_e in the laboratory frame. The horizontal white line in panels (b), (c), (g) and (h) show the position at which the slices were extracted. The bottom panels (d), (e), (i) and (j) show the N_e distribution in the laboratory frame.

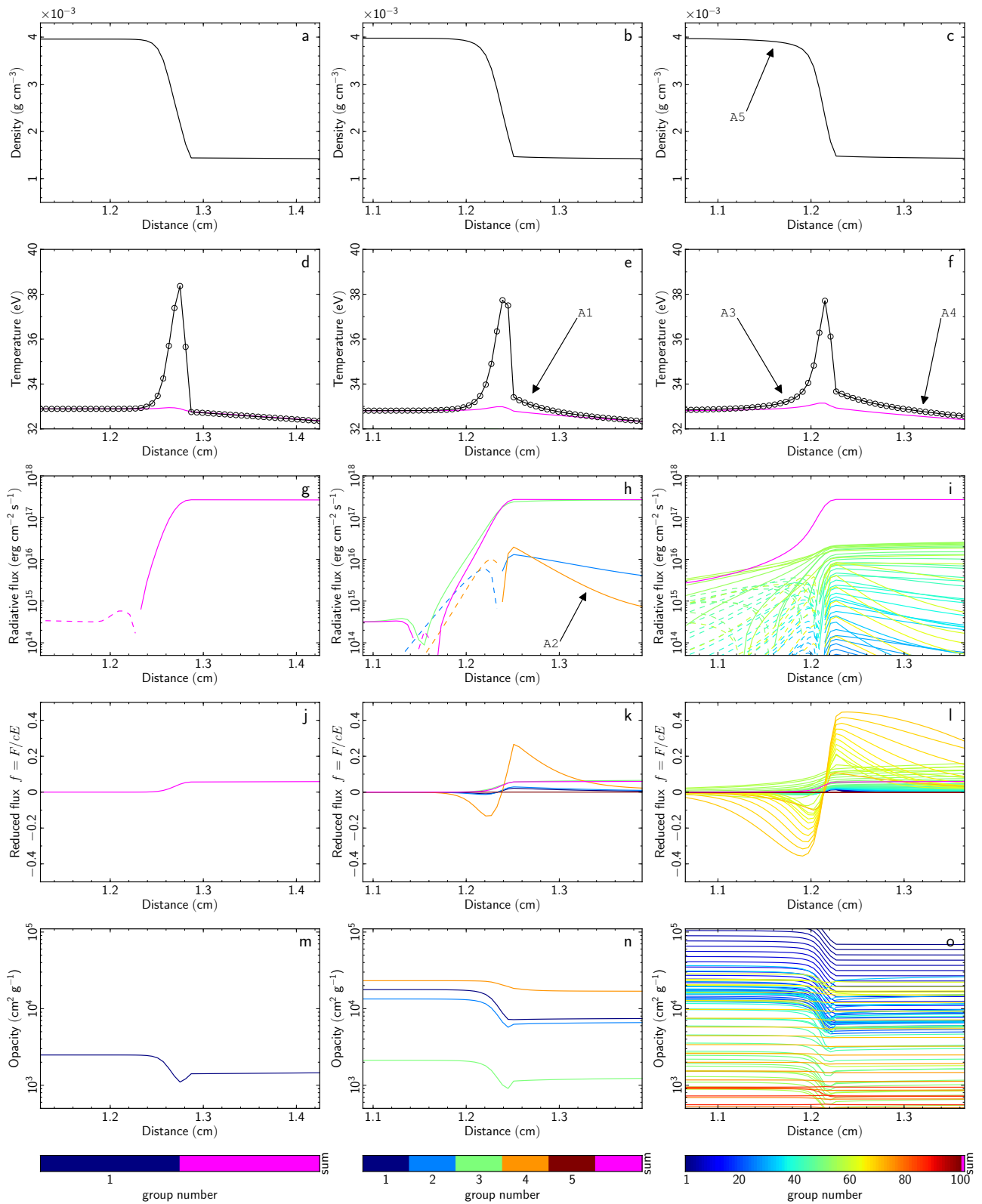


Figure 7: A close-up view on the region around the Zel'dovich temperature spike for runs SUP001 (left), SUP005 (center) and SUP100 (right). From top to bottom: gas density, gas (black) and radiative (magenta) temperature, radiative flux, reduced flux and gas opacity. In the temperature panels, the circles indicate the grid cells. As in the previous figures, the magenta curves represent the radiative quantities summed over all groups and the dashed lines symbolise negative values of the radiative flux.

In one dimension, integrating over frequency and solid angle this reduces to

$$\begin{aligned} E^{\text{abs}} &= \int_0^\infty \kappa_\nu \int_{-1}^{+1} \mu I_\nu d\mu \, d\nu \, dA \, dt \, ds \\ &= \int_0^\infty \kappa_\nu F_\nu \, d\nu \, dA \, dt \, ds \end{aligned} \quad (12)$$

where μ is the direction cosine. So the energy absorbed is proportional to $\int_0^\infty \kappa_\nu F_\nu \, d\nu$. We now suppose that we have two frequency groups, and to mimic the situation in run SUP005, we define the group quantities in the following way. The two groups have the same width in the frequency dimension $\Delta\nu$, and we further assume the radiative flux and gas opacity to be constant within each group, i.e. $\int_0^\infty \kappa_\nu F_\nu \, d\nu = \sum_g \kappa_g F_g \Delta\nu$. The first group can be compared to group 3 in SUP005; it dominates the radiative energy and flux, but has small reduced flux and opacity. On the other hand, the second group has a small energy and flux, but a large opacity and reduced flux (similar to group 4 in SUP005). We choose

Group 1 :	Group 2 :
$E_1 = E_0$	$E_2 = E_0/100$
$\kappa_1 = 0.1$	$\kappa_2 = 1.0$
$f_1 = 0.05$	$f_2 = 0.5$
$F_1 = 0.05cE_0$	$F_2 = 0.005cE_0$

The integral over the frequency range in equation (12) now becomes a sum over the two groups and we have

$$\begin{aligned} E^{\text{abs}} &\propto [\kappa_1 F_1 + \kappa_2 F_2] \Delta\nu \\ &\propto [5 \times 10^{-3} cE_0 + 5 \times 10^{-3} cE_0] \Delta\nu \end{aligned} \quad (13)$$

which is twice as much as what is found by considering only the dominant group 1. This shows that a group with very little radiative energy and radiative flux can contribute significantly to the total energy absorbed if it has a large reduced flux and opacity. The fact that $E_1/E_2 = 100$ means that including group 2 does not change the total radiative temperature, but does change the amount of energy absorbed by the gas, and the gas and radiative temperatures can hence be decoupled.

The morphology of the Zel'dovich spike changes again for run SUP100 (Fig. 7f). The decoupled regions both to the left and the right of the hydrodynamic discontinuity are wider than for SUP005 (see arrows A3 and A4). The radiative flux diagram (i) this time shows more components with a noticeable downward trend and large reduced fluxes. The range of opacities in the numerous groups mean that the radiation in different groups are absorbed at different rates, which yields a wider relaxation region to the right of the shock. The same effect is also observed to the left of the spike where the gas and radiation temperatures are also decoupled (with negative fluxes travelling from right to left).

The structure observed here is what is described as an adaptation zone by Drake (2007a,b); a region across which the influence of radiation from the cooling layer on the shock structure fades away and where the temperature and other

gas quantities make their final small adjustments in order to reach their final steady-state values. Figure 1 in Drake (2007a) actually depicts exactly the situation we observe here. There are two adaptation zones on each side of the cooling layer (i.e. the Zel'dovich spike) where the gas temperature is higher than the final state T_1 downstream of the density discontinuity and higher than the precursor temperature T_- upstream. This is precisely what our simulation results show for 10 frequency groups and above. Drake (2007a) actually depicts the pre-shock temperature just before the discontinuity as below or equal to the final state T_1 , but he does mention that ‘‘ongoing numerical work by John Castor suggests that the temperature inside the adaptation zone, at the actual density jump, may be pulled up above $[T_1]$ ’’.

The extent of the region inside which the radiative flux from the cooling layer still has an effect on the surrounding gas will inevitably depend on the opacity of the gas, which explains the different observed sizes for the adaptation zones as we vary the number of groups. The density is also pictured in Drake’s papers as being slightly lower than the final state ρ_1 inside the downstream adaptation zone and higher than the leftmost precursor value ρ_- in the upstream zone. This is also the case in our results, as shown by arrow A5 in Fig. 7c.

Drake (2007b) provide an analytical estimate of the width of the spike for a given shock strength, and when applied to our simulation setup, it predicts that the spike should be narrower by a factor ~ 30 . McClarren & Drake (2010) also mention that the M_1 model, even though it describes the total energy flows correctly, might not perform satisfactorily in the vicinity of the cooling layer, but this has yet to be investigated. It would appear from the analytical estimates that we might not be resolving the real ‘physical’ Zel'dovich spike, but the discussion in Appendix B shows that we are sufficiently resolving the spike (for the purpose of this study) resulting from our numerical model. We also demonstrate that our observation of adaptation zones being absent from grey simulations while being clearly detected in multigroup simulations is not resolution dependent. While we have to acknowledge that we might not be resolving the true width of the spike, as we do not attempt to make any comparisons with experiments, we believe that our results are still legitimate.

Finally, the presence of these adaptation zones in our simulations forces us to revise our depiction of a radiative shock structure and adopt a more up-to-date description (see Fig. 8). The preshock gas is heated by the radiative precursor to a temperature $T_- \approx T_1$, and increases slightly to a temperature T_r as we cross the right adaptation zone through radiative heating. The shock compression at the density jump (discontinuity) heats it further to a temperature T_+ which is higher than the final post-shock equilibrium state T_1 . The gas then cools down inside the cooling layer to reach the intermediate post-shock state T_l by radiating the excess energy away. The final small adjustments are made across the left adaptation zone to reach the final post-shock state T_1 (see also Drake 2007b). The radiative temperature

(dotted line) is equal to the gas temperature for the most part, except that it remains constant across the cooling layer and the adaptation zones (decoupled from the gas), and is higher than the gas temperature inside the transmissive precursor. The pressure gradient at the head of the precursor, through the conservation of mass (4) and momentum (5), causes the velocity to decrease and the density to increase to a value ρ_- ahead of the discontinuity. Since the gas temperature is close to being constant in the diffusive part of the precursor, there is no more pressure gradient and the density reaches a plateau value ρ_- ahead of the discontinuity. A small compression from ρ_- to ρ_r occurs as we cross the right adaptation zone, then followed by the sharp density jump of the shock from ρ_- to ρ_+ which takes place on the gas viscous scale. The density then rises rapidly to ρ_l inside the cooling layer through strong contraction of the radiating gas. Lastly, the density slowly reaches the final state ρ_1 across the left adaptation zone.

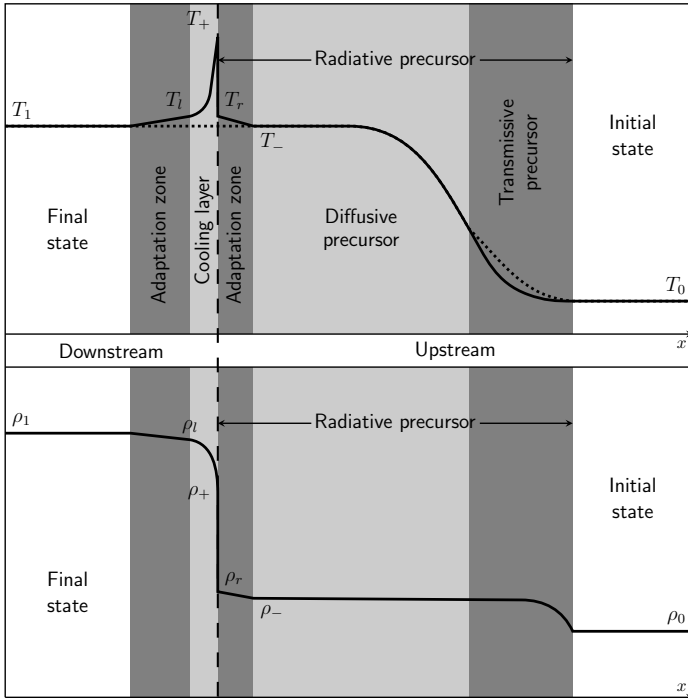


Figure 8: Structure of a supercritical radiative shock (adapted from Drake 2007a). The direction of the gas flow is from right to left in the frame where the shock is at rest. Top panel: gas (solid) and radiative (dotted) temperature as a function of distance. Bottom panel: gas density as a function of distance. The position of the temperature and density jumps is marked by the vertical dashed line. The relative sizes of the layers are for illustration purposes only.

3.5 Hugoniot curves

In this section we look at the Hugoniot curves for gas velocity, pressure and radiative flux in our simulations. The Hugoniot curves are analytical predictions for the state of gas quantities as a function of the inverse compression ratio $\eta = \rho_0/\rho$ for which conservation of mass, momentum and

energy hold (see Zel'dovich & Raizer 1967; Mihalas & Mihalas 1984, for example). Figure 9 shows (from top to bottom) the gas velocity, pressure and radiative flux as a function of inverse compression ratio for every grid point in our subcritical (left) and supercritical (right) simulations, as well as the analytical solutions (solid black line) which are

$$u(\eta) = -u_0\eta \quad (14)$$

$$p(\eta) = \rho_0 u_0^2 (1 - \eta) + p_0 \quad (15)$$

$$F(\eta) = \frac{\rho_0 u_0^3}{2} \left(\frac{2\gamma}{\gamma-1} \eta - \frac{\gamma+1}{\gamma-1} \eta^2 - 1 \right) - \frac{\gamma p_0 u_0}{\gamma-1} (1 - \eta) + F_0 \quad (16)$$

where γ is the ratio of specific heats and the radiative flux F is expressed in the laboratory frame (note that we have converted our radiative quantities to the laboratory frame using equations 91.16 and 91.17 in Mihalas & Mihalas 1984).

This illustrates well how our numerical scheme preserves the important physics of conservation of mass, momentum and energy. Any simulation of shocks which has points lying away from these analytical curves does not conserve these fundamental quantities. The points which do not lie on the analytical curves in Fig. 9 are all in the shock transition region which is inevitably spread over a minimum number of cells for a Godunov method and do not strictly match the analytical solution (see Sincell et al. 1999; Drake 2007b, for example). This is mostly visible in the subcritical case where the radiative flux follows a constant value transition while the gas velocity and pressure follow an approximate Hugoniot curve through the transition to connect the upstream and downstream states. Note that only a single cell for each simulation does not lie on the analytical prediction, illustrating the fact that the transition is spread over only one or two grid cells. We take the opportunity here to point out that the comoving frame formalism, which has been criticized in several works for not rigorously conserving the total energy (see Mihalas & Klein 1982; Krumholz et al. 2007, for example), appears here to perform very well in conserving the fundamental quantities.

4 Conclusions

We have performed simulations of stationary radiative shocks in Ar gas using a multigroup radiation hydrodynamics scheme. Gas opacities depending on temperature, density and frequency were used in the equations of radiation hydrodynamics to achieve convincing results. The simulations reproduced all the detailed structure of a radiative shock, including the radiative precursor, the cooling layer and even the adaptation zones connecting the cooling layer to the final downstream state and the precursor. Our results show that grey simulations produce very different results compared to multigroup ones, and that frequency-independent calculations are not deemed an accurate description of the problem. Indeed, multigroup simulations showed increases by a factor of four in precursor size in the subcritical case, and an increase of 20% in the supercritical case. The simulations with 5 to 100 groups also show

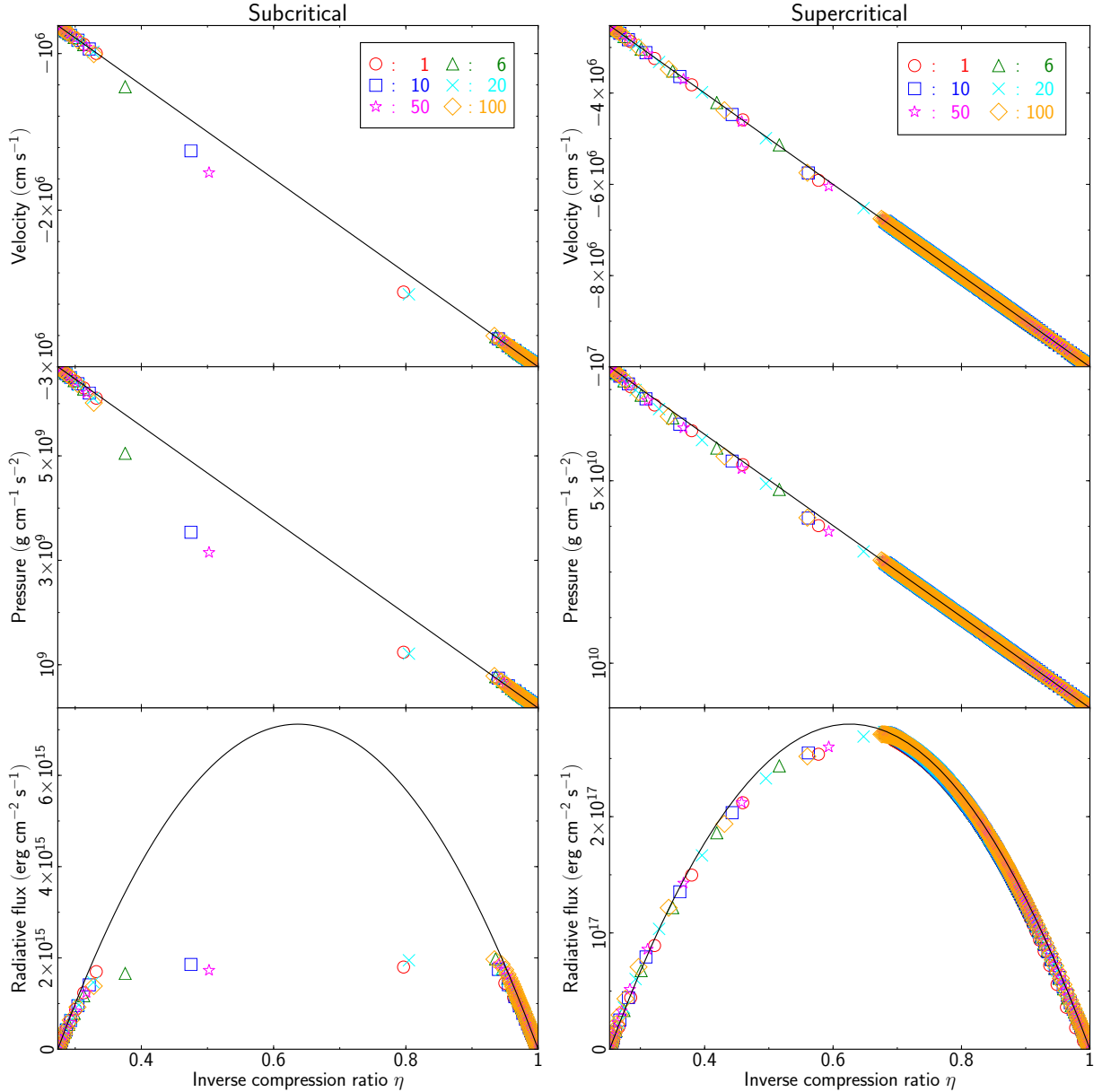


Figure 9: Hugoniot curves for the radiative shock simulations using 1 – 100 frequency groups (see legend in the top right corner for the meaning of the symbols): gas velocity (top), pressure (middle) and radiative flux (bottom) as a function of inverse compression ratio in the case of the subcritical shock (left column) and the supercritical shock (right column). The analytical solutions are overlaid for comparison (black solid line). The simulation points not lying on the analytical solutions are all within the shock transition.

increasing precursor sizes, with a suspected convergence of results for 50 groups and above. Multigroup effects were also seen to be important in the vicinity of the cooling layer, where adaptation zones absent from grey simulations were clearly detected.

We have to acknowledge that several caveats need to be taken into account when considering the results reported in this work. Firstly, the exact sizes of the radiative precursors are not entirely correct since higher resolution simulations reported in Appendix B yield slightly different results (typical differences are of the order of 5 – 10%), only the relative increase in precursor sizes between the different simulations

are of notorious relevance. Secondly, even though our results are numerically quantitatively converged in the proximity of the Zel’dovich spike, it is not clear whether the M_1 model performs accurately enough on such small scales. We remind the reader that this work is not an attempt at directly comparing numerical simulations to experiments, merely a study of the effects of frequency dependence on the results of radiation hydrodynamic calculations.

Nevertheless, the findings presented still have important consequences on predictions made by numerical simulations on the structure of radiative shocks. Indeed, studies of astrophysical (accretion processes, supernova remnants, jets,

etc. . .) or laboratory radiative shocks will most probably be inaccurate if a grey radiative transfer model is used. The impact can not only be large when looking at the radiative precursor sizes, but also on the total energy budget, determining the amount of energy converted into radiation and absorbed by pre-shock material.

It is difficult to compare the results of this work with experimental data directly since our idealised setup of stationary radiative shocks is very far from the situation in laboratories where laser-driven radiative shocks travel through gas chambers and it is often unclear if they ever reach a stationary state. Realistic calculations using a piston-like shock-driving boundary, as well as a more sophisticated equation of state, will be more appropriate for conducting detailed modelling of laboratory experiments.

Acknowledgements

The research leading to these results has received funding from the European Research Council under the European Community's Seventh Framework Programme (FP7/2007-2013 Grant Agreement no. 247060). The authors also gratefully acknowledge support from grant ANR-06-CIS6-009-01 for the programme SiNeRGHy. The authors would also like to thank M. Busquet for fruitful discussions which have yielded vast improvements of this paper and J. P. Gauthier for the Ar opacity tables. Finally, the authors would like to thank the reviewers for very useful comments which have helped greatly in improving the robustness and credibility of the paper.

References

- Blinnikov, S. I., Tolstov, A. G., 2011, *Astronomy Letters*, 37, 194
- Bode, M. F., Evans, A., 2008, *Classical Novae*, 2nd Edition. Ed. M.F. Bode and A. Evans., Cambridge Astrophysics Series, No. 43, Cambridge: Cambridge University Press
- Bozier, J. C., Thiell, G., Le-Breton, J. P., Azra, S., Decroisette, M., Schirmann, D., 1986, *Phys. Rev. Lett.*, 57, 1304
- Bouquet, S., Stéhlé, C., Koenig, M., et al., 2004, *Physical Review Letters*, 92, 225001
- Busquet, M., Audit, E., Gonzalez, M., Stehle, C., Thais, F., Acef, O., Bauduin, D., Barroso, P., Rus, B., Kozlova, M., Polan, J., Mocek, T., 2007, *High Energy Density Physics*, 3, 8
- Commerçon, B., Audit, E., Chabrier, G., Chièze, J.-P., 2011, *Astron. & Astrophys.*, 530, A13
- Draine, B. T., McKee, C. F., 1993, *Annu. Rev. Astron. Astrophys.*, 31, 373
- Drake, R. P., 2006, *High Energy Density Physics: Foundations, Inertial Fusion, and Experimental Astrophysics*, Chapter 7.4, Berlin: Springer
- Drake, R. P., 2007a, *IEEE Trans. on Plasma Science*, 35, 171
- Drake, R. P., 2007b, *Phys. Plasmas*, 14, 043301
- Dubroca, B., Feugeas, J.-L., 1999, *C. R. Acad. Sci. Paris*, 329, 915
- Edwards, M. J., MacKinnon, A. J., Zweiback, J., Shigemori, K., Ryutov, D. D., Rubenchik, A. M., Keittly, K. A., Liang, E., Remington, B. A., Ditmire, T., 2001, *Phys. Rev. Lett.*, 87, 085004-1
- Fadeyev, Y. A., Gillet, D., 2000, *Astron. & Astrophys.*, 354, 349
- Falize, E., Michaut, C., Cavet, C., Bouquet, S., Koenig, M., Loup, B., Ravasio, A., Gregory, C. G., 2009, *Astrophys. & Space Science*, 322, 71
- Fleury, X., Bouquet, S., Stehlé, C., Koenig, M., Batani, D., Benuzzi-Mounaix, A., Chièze, J.-P., Grandjouan, N., Grenier, J., Hall, T., Henry, E., Lafon, J.-P., Leygnac, S., Malka, V., Marchet, B., Merdji, H., Michaut, C., Thais, F., 2002, *Laser and Particle Beams*, 20, 263
- Ghavamian, P., Raymond, J., Hartigan, P., Blair, W. P., 2000, *Astrophys. J.*, 535, 266
- Gillet, D., 2006, *EAS Publications Series*, 21, 297
- González, M., Stehlé, C., Audit, E., Busquet, M., Rus, B., Thais, F., Acef, O., Barroso, P., Bar-Shalom, A., Bauduin, D., Kozlova, M., Lery, T., Madouri, A., Mocek, T., Polan, J., 2006, *Laser Part. Beams*, 24, 535
- González, M., Audit, E., Huynh, P., 2007, *Astron. & Astrophys.*, 464, 429
- González, M., Audit, E., Stehlé, C., 2009, *Astron. & Astrophys.*, 497, 27
- Imamura, J. N., 1985, *Astrophys. J.*, 296, 128
- Keiter, P. A., Drake, R. P., Perry, T. S., Robey, H. F., Remington, B. A., Iglesias, C. A., Wallace, R. J., Knauer J., 2002, *Phys. Rev. Lett.* 89, 165003
- Krumholz, M., Klein, R. I., McKee, C. F., Bolstad, J., 2007, *Astrophys. J.*, 667, 626
- Larsen, J. T., Lane, S. M., 1994, *JQSRT*, 51, 179
- Leibrandt, D. R., Drake, R. P., Reighard, A. B., Glendinning, S. G., 2005, *Astrophys. J.*, 626, 616
- Levermore C. D., 1984, *JQSRT*, 31, 149
- Lowrie, R. B., Rauenzahn, R. M., 2007, *Shock Waves*, 16, 445
- Lowrie, R. B., Edwards, J. D., 2008, *Shock Waves*, 18, 129
- McClarren, R. G., Drake, R. P., 2010, *JQSRT*, 111, 2095
- Michaut, C., Falize, E., Cavet, C., Bouquet, S., Koenig, M., Vinci, T., Reighard, A., Drake, R. P., 2009, *Astrophys. & Space Science*, 322, 77
- Mihalas, D., Klein, R. I., 1982, *Journal of Computational Physics*, 46, 97
- Mihalas, D., Mihalas, B. D., 1984, *Foundations of Radiation Hydrodynamics*, New York: Oxford University Press
- Mirone, A., Gauthier, J. C., Gilleron, F., Chenais-Popovics, C., 1997, *JQSRT*, 58, 791
- Nymark, T. K., Fransson, C., Kozma, C., 2006, *Astron. & Astrophys.*, 449, 171
- Offner, S. S. R., Klein, R. I., McKee, C. F., Krumholz, M. R., 2009, *ApJ*, 703, 131
- Orlando, S., Drake, J. J., Laming, J. M. 2009, *Astron. & Astrophys.*, 493, 1049
- Pomraning, G. C., 1973, *International Series of Monographs in Natural Philosophy*, Oxford: Pergamon Press
- Raga, A. C., Mellema, G., Arthur, S. J., Binette, L., Ferruit, P., Steffen, W., 1999, *Rev. Mex. Astron. Astrofis.*, 35, 123
- Reighard, A. B., Drake, R. P., Dannenberg, K. K., et al., 2006, *Physics of Plasmas*, 13, 082901
- Reighard, A. B., Drake, R. P., Mucino, J. E., Knauer, J. P., Busquet, M., 2007, *Physics of Plasmas*, 14, 056504
- Reipurth, B., Raga, A. C., 1999, *NATO ASIC Proc. 540: The Origin of Stars and Planetary Systems*, 267
- Sampson, D., 1965, *JQSRT*, 5, 211
- Shestakov, A. I., Offner, S. S. R., 2008, *JCP*, 227, 2154
- Sincell, M. W., Gehmeyr, M., Mihalas, D., 1999, *Shock Waves* 9, 391
- Stahler, S. W., Shu, F. H., Taam, R. E., 1980, *Astrophys. J.*, 241, 637
- van der Holst, B., Toth, G., Sokolov, I. V., Powell, K. G., Holloway,

- J. P., Myra, E. S., Stout, G., Adams, M. L., Morel, J. E., Drake, R. P., 2011, *ApJS*, 194, 23
- Vaytet, N. M. H., O'Brien, T. J., Bode, M. F., 2007, *Astrophys. J.*, 665, 654
- Vaytet, N. M. H., Audit, E., Dubroca, B., Delahaye, F., 2011, *JQSRT*, 112, 1323
- Zel'Dovich, Y. B., Raizer, Y. P., 1967, *Physics of shock waves and high temperature hydrodynamic phenomena*, New York: Academic Press
- Zhang, W., Howell, L., Almgren, A., Burrows, A., Dolence, J., Bell, J., 2013, *ApJS*, 204, 7

A Using the correct opacity average

In the RHD equations (5)–(8), it is challenging to compute the radiative energy and flux-weighted mean opacities κ_E and κ_F (note that $\sigma = \kappa\rho$), since the quantities E_v and F_v are not necessarily known at *all* wavelengths. The choice of approximation for these quantities, which are crucial to the RHD calculations, is not trivial (see Pomraning 1973, p. 88+ for a discussion). Common practise is to set $\kappa_E = \kappa_P$ and $\kappa_F = \kappa_R$ where κ_P and κ_R are the Planck and Rosseland mean opacities, respectively (see Larsen & Lane 1994; Offner et al. 2009, for example). However, for the M_1 model, numerical stability is immensely improved if an identical value for κ_E and κ_F is used, which prompts us to use an average value $\kappa_{av} = \kappa_E = \kappa_F$.

The Planck and Rosseland means are applicable to different regimes. In the diffusion limit, the opacity should be equal to the Rosseland mean, while the Planck mean is appropriate in the free-streaming limit. We need to make sure that we recover this behaviour with our average opacity. Sampson (1965) proposed an average which varies between κ_P and κ_R depending on the optical depth. Here, we use the reduced radiative flux $f = \|\mathbf{F}\|/cE$ as a measure of the diffusivity (optically thick) or transmissivity (optically thin) of the flow. We define a parameter $a(f)$ which varies between zero and one according to f which then allows us to write the average opacity

$$\kappa_{av} = (1 - a)\kappa_R + a\kappa_P. \quad (17)$$

In order to recover the diffusion and free-streaming limits, a needs to have the following properties: $a \rightarrow 0$ when $f \rightarrow 0$ and $a \rightarrow 1$ when $f \rightarrow 1$. The simplest formula with these properties is just the linear function $a = f$. However, we argue that the a parameter is meant to represent the transition from a regime dominated by diffusion to a radiation-dominated regime. In this sense, one expects the transition from one to the other to be rather rapid, as opposed to a smooth linear averaging between the κ_P and κ_R values. We thus propose a different formula for a which will better reproduce this behaviour. After some experimenting, we finally chose

$$a_s = \frac{1}{e^{-15(f-1/2)} + 1} \quad (18)$$

which is plotted in Fig. 10 (red) alongside the simpler $a = f$ (black). We would like to point out here that we have no physical explanation for equation (18), it is simply an *ad-hoc*

choice of a function with the correct properties. However, we can justify our choice by testing the method in a simple case.

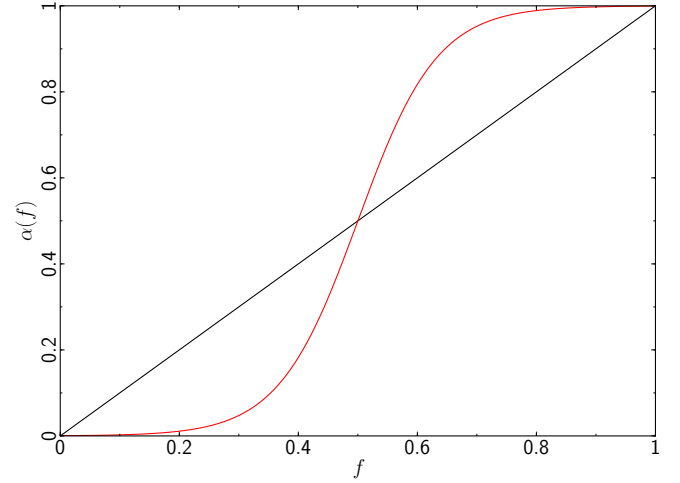


Figure 10: a parameter as a function of reduced flux f : the black solid line is the simple $a = f$ while the red line is given by equation (18).

We performed eight simulations with a single frequency group; four calculations of a subcritical radiative shock and four of a supercritical shock. In each case, the first was carried out using $a = f$, the second using $a = a_s$, the third using $a = 0$ (which corresponds to $\kappa_{av} = \kappa_R$) and the fourth using $a = 1$ ($\kappa_{av} = \kappa_P$). We show the results in Fig. 11. In the case of the subcritical radiative shock (left column), we see that the average opacities (black and red) are equal to the Rosseland mean far away from the discontinuity (on both sides). They then become close to the Planck average in the intermediate region (between 0.25 and 0.28 cm) where the reduced flux is large. The temperature plot shows that the results for both the averaging schemes are very close to the blue curve (Planck mean) which is the desired result in this optically thin regime. For the supercritical shock (right column), the average opacity should produce results which resemble the green curves, which are appropriate in this diffusive regime (only a small region of the grid has a large f). This time, the simple $a = f$ approximation shows its limitations with a precursor size about two thirds of the size of the one observed in the $\kappa_{av} = \kappa_R$ case. On the other hand, the $a = a_s$ model performs much better, producing results very similar to the $\kappa_{av} = \kappa_R$ simulation. We thus conclude that the expression given in equation (18) is an effective model to simulate problems in both diffusive and free-streaming limits.

In a final note, we wish to reiterate that the inaccuracies which arise from the approximation of setting $\kappa_E = \kappa_F = \kappa_{av}$ are reduced as the number of frequency groups used increases, since in the limit of infinite frequency resolution, all of these quantities simply reduce to κ_v . This approximation is thus less crude in a multigroup model than in a grey model.

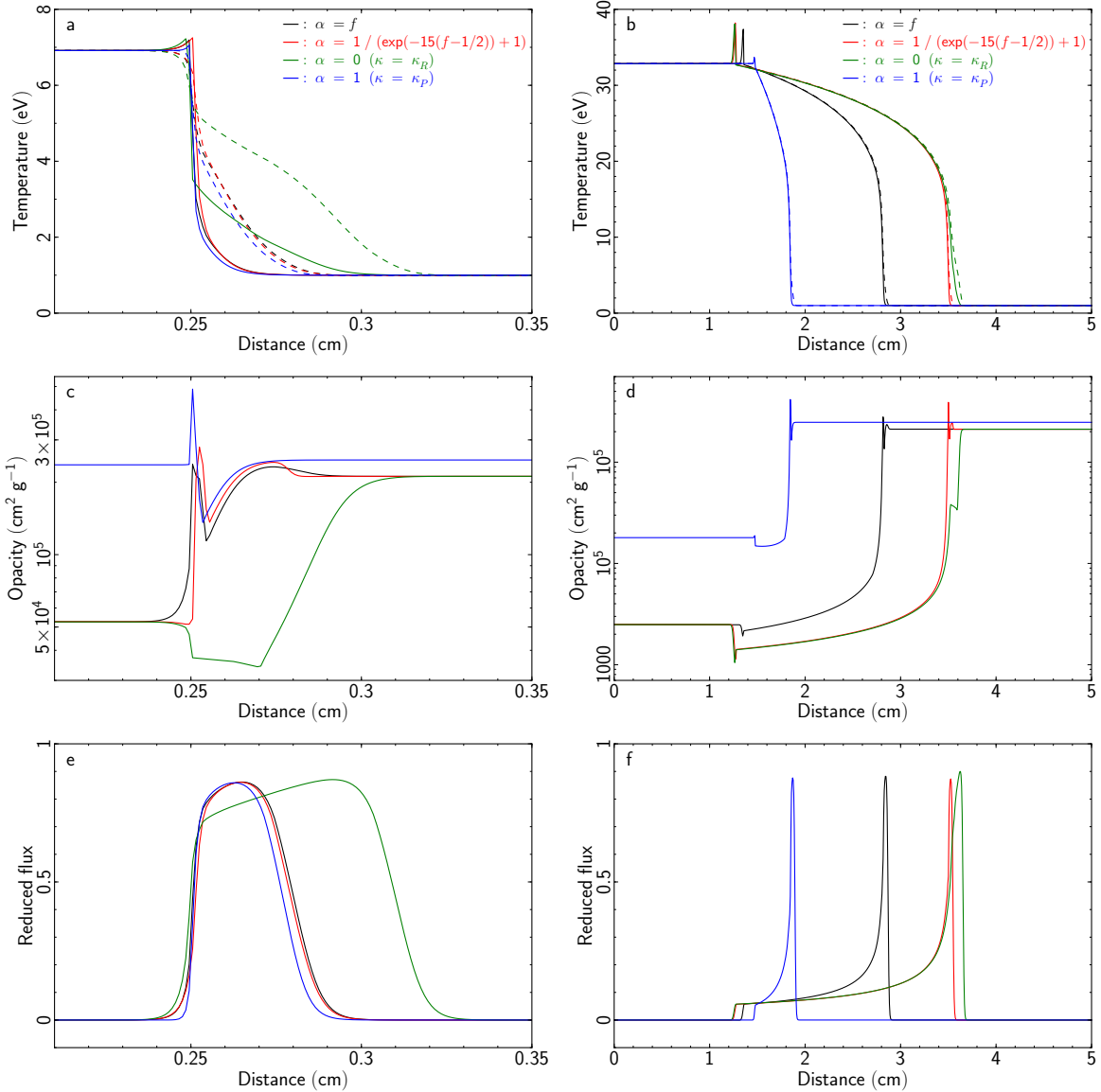


Figure 11: Comparison of the different opacity averaging functions. The left and right columns show the results for the subcritical and supercritical radiative shocks, respectively. The top row displays the gas (solid) and radiative (dashed) temperatures, the middle row is the gas opacity and the bottom row shows the reduced flux. The colour-coding is as follows: black is for $a = f$, red is for a given by equation (18), green is for $\kappa_{\text{av}} = \kappa_R$ and blue is for $\kappa_{\text{av}} = \kappa_P$.

B A comment on spatial resolution

In Fig. 7 it would appear that with our spatial resolution of 1000 grid cells, we do not fully resolve the very narrow Zel’dovich spike. For completeness, we report in this section a short spatial resolution study to confirm that our results concerning the influence of the number of frequency groups on the size of the radiative precursors and adaptation zones on each side of the spike are robust. Figure 12 compares the effects of grid resolution and number of frequency groups on the shock structures. The top row shows the temperature profiles in the vicinity of the cooling layer for 1 frequency group using 500, 1000, 5000 and 10,000 cells in the subcritical (a) and supercritical (b) cases (see color key at the top of the figure). In the subcritical case, the different reso-

lutions appear to yield similar results. For the supercritical runs, the spike appears well resolved in the high resolution simulations. It looks thinner than in the lower resolution calculations and displays a (smooth) maximum to the left of the discontinuity, a structure that much resembles the results of Lowrie & Edwards (2008). At a Mach number of ~ 19 , the spike structure fits well between their depictions of shocks at $M = 3$ (Fig. 10) and $M = 27$ (Fig. 13). A strong convergence of results is observed between 5000 and 10,000 cells.

The middle row shows again the temperature profiles of the cooling layer for different resolutions but this time using 5 frequency groups. Panel (c) reveals that 500 cells is most probably too few to resolve the cooling layer. Both panels also show convergence between 5000 and 10,000 cells. More

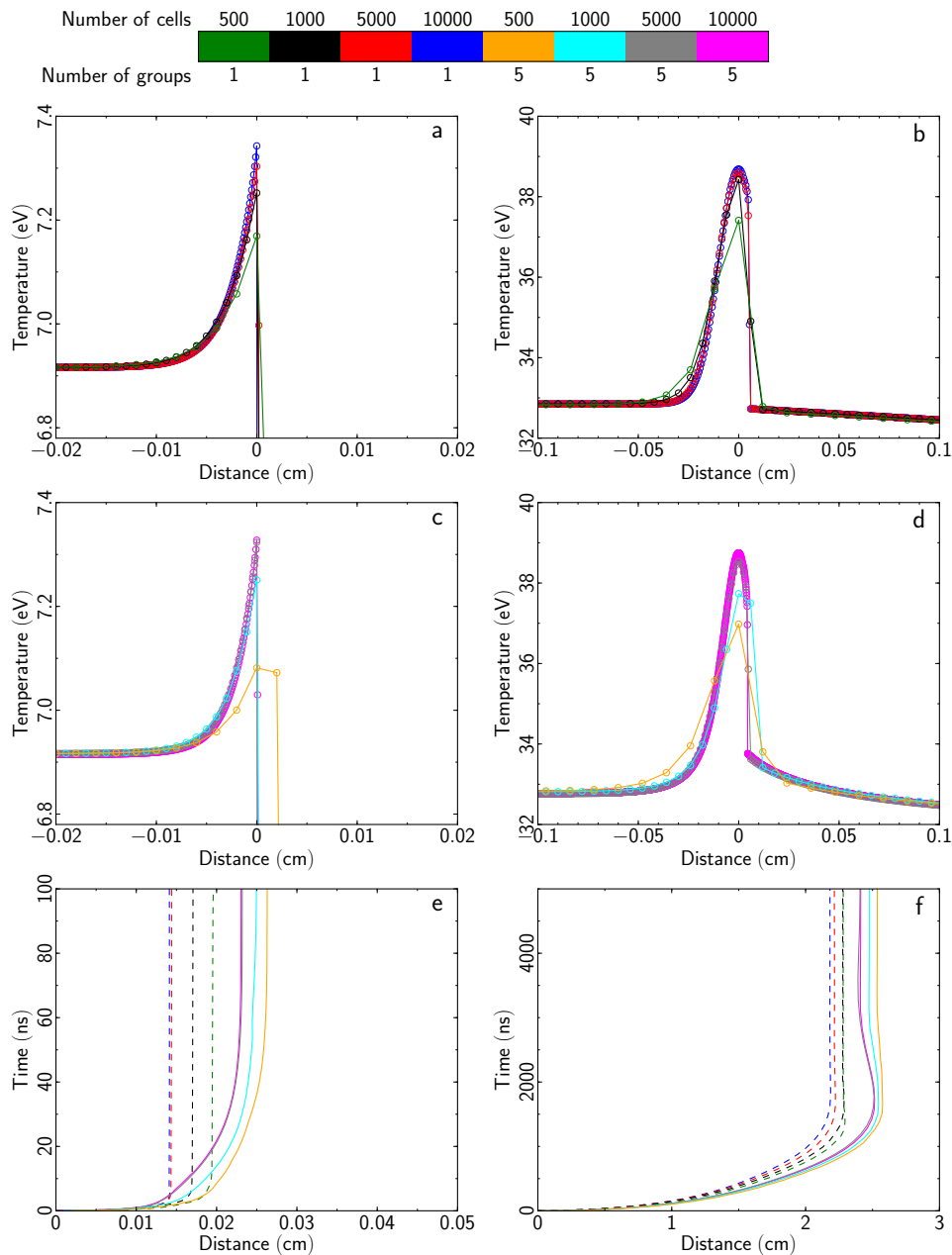


Figure 12: Comparison between the effects of grid resolution and number of frequency groups. Top row: temperature profiles in the vicinity of the cooling layer for 1 frequency group using different spatial resolutions in the subcritical (a) and supercritical (b) cases (see color key at the top of the figure). Middle row: same as the top row but using 5 frequency groups. Bottom row: size of precursor as a function of time for the 1-group (dashed) and 5-groups (solid) simulations in the subcritical (e) and supercritical (f) cases.

importantly, panels (b) and (d) demonstrate that our overall conclusions on the presence of adaptation zones in the multigroup simulations remain. Even though the relaxation region to the right of the spike is more pronounced in the 5000-cell simulation (grey), the results from the 1000-cell simulations (cyan) agree qualitatively; an adaptation zone is absent from the grey simulations but is detected in the multigroup simulations.

Analytical estimates of the width of the spike from Drake (2007b) suggest that the real physical spike for the same val-

ues of shock velocity and initial state density might in fact be much narrower (by a factor of ~ 30). Nevertheless, the fact remains that we have converged spatially on the structure of the cooling layer given by our M_1 model, which is what matters for the present study. In addition, analytical estimates also make use of approximations and the *true* width of the spike is probably not known accurately.

The bottom row displays the size of the radiative precursors as a function of time for the different simulations. To better distinguish the separate runs, we have plotted the

simulations using 1 group with dashed lines and the simulations using 5 groups with solid lines (the colours remain the same as in the other panels). These plots reveal that the spatial resolution also affects the total size of the precursor (here again the results have converged for 5000 cells and above). However, as we do not make any direct comparisons with experiments or observations throughout this work but are only interested in the relative differences in precursor sizes, we argue that our conclusions regarding the increase in precursor size as a function of number of frequency groups remain qualitatively correct. Moreover, panels (e) and (f) show quite clearly that the difference in precursor size due to a change in number of groups is larger than the difference observed from a change in number of cells. In addition, Fig. 12 only shows the results using 1 and 5 groups, and the size of the

precursor is seen to continue increasing all the way up to 100 groups (see Fig. 4). In the case of the subcritical shock, differences between runs with 1000 and 10,000 cells are $\sim 20\%$ and $\sim 8\%$ for the 1-group and 5-groups simulations, respectively, while differences between the 1-group and 100-groups (1000 cells) simulations are higher than 400% (see Table 1). As for the supercritical, resolution alters the precursor sizes by only 2 – 4% while frequency groups have an effect of the order of 20%. Finally, the relative differences in precursor size between 1- and 5-group simulations for a given resolution remain approximately constant. It was not possible for us to run a 100-group simulation using 5000 cells on a realistic timescale, but we believe that the results of the 1000-cell simulations are qualitatively robust.